International Journal of Mass Spectrometry 288 (2009) 58–67

Contents lists available at ScienceDirect

International Journal of Mass Spectrometry

journal homepage: www.elsevier.com/locate/ijms

# Off-axis field approximations for ion traps with apertures

Madhurima Chattopadhyay[a], Atanu K. Mohanty[a,b,*]

[a] Department of Instrumentation, Indian Institute of Science, Bangalore 560012, India
[b] Supercomputer Education and Research Centre, Indian Institute of Science, Bangalore 560012, India

ARTICLE INFO

*Article history:*
Received 19 June 2009
Received in revised form 11 August 2009
Accepted 12 August 2009
Available online 25 August 2009

*Keywords:*
Axially symmetric (3D) trap
Two dimensional (2D) trap
Boundary element method (BEM)
Electric field in the vicinity of aperture
Multipole

ABSTRACT

In recent work (*Int. J. Mass Spec.*, vol. 282, pp. 112–122) we have considered the effect of apertures on the fields inside rf traps at points on the trap axis. We now complement and complete that work by considering *off-axis* fields in axially symmetric (referred to as "3D") and in two dimensional ("2D") ion traps whose electrodes have apertures, i.e., holes in 3D and slits in 2D. Our approximation has two parts. The first, $E_{\text{noAperture}}$, is the field obtained numerically for the trap under study with apertures artificially closed. We have used the boundary element method (BEM) for obtaining this field. The second part, $E_{\text{dueToAperture}}$, is an analytical expression for the field contribution of the aperture.

In $E_{\text{dueToAperture}}$, aperture size is a free parameter. A key element in our approximation is the electrostatic field near an infinite thin plate with an aperture, and with different constant-valued far field intensities on either side. Compact expressions for this field can be found using separation of variables, wherein the choice of coordinate system is crucial. This field is, in turn, used four times within our trap-specific approximation.

The off-axis field expressions for the 3D geometries were tested on the quadrupole ion trap (QIT) and the cylindrical ion trap (CIT), and the corresponding expressions for the 2D geometries were tested on the linear ion trap (LIT) and the rectilinear ion trap (RIT). For each geometry, we have considered apertures which are 10%, 30%, and 50% of the trap dimension. We have found that our analytical correction term $E_{\text{dueToAperture}}$, though based on a classical small-aperture approximation, gives good results even for relatively large apertures.



## 1. Introduction

This paper complements and completes our recent work [5], and presents approximate analytical expressions for *off-axis* fields in axially symmetric (referred to as 3D) and two dimensional (2D) ion trap mass analyzers with apertures in their electrodes. The expression for the field we present has two parts. One part is the numerically obtained field for the trap with apertures artificially closed. The second term is an analytical expression for the contribution of the apertures to the field within the trap. In particular, we present electrostatic field solutions for infinite thin plates with finite apertures, followed by multiple applications of the same to account for nonzero-sized apertures in two endcaps, each of nonzero thickness. Final results obtained are accurate even for apertures of significant size in comparison to trap dimensions.

Axially symmetric (3D) mass analyzers, such as the quadrupole ion trap or QIT [11] and the cylindrical ion trap or CIT [9,16], have a three electrode geometry consisting of a central ring electrode and two endcap electrodes. In the QIT, all electrodes have hyperboloid shapes, while the CIT has a simplified geometry with planar endcaps and cylindrical ring electrode. Trapping of ions of an analyte gas is achieved in the central cavity by application of an rf/dc or rf-only potential between the ring and the electrically shorted endcap electrodes. The endcap electrodes have holes in them to permit entry of electrons (for ionizing the analyte gas) and for collection of destabilized ions.

Examples of 2D mass analyzers are the linear ion trap or LIT [3] and the rectilinear ion trap or RIT [10]. These consist of four parallel longitudinal electrodes, the two opposite pairs being electrically shorted. In the LIT, the electrodes have hyperbolic shapes while in the RIT the electrodes are flat plates. Ion trapping in these mass analyzers is achieved by applying an rf/dc or rf-only potential across the two pairs of electrodes, the trapped ions being confined along the axis of the mass analyzer. Here too, one pair of electrodes have slits in them to permit electron entry and collection of destabilized ions.

In conventional commercial mass analyzers, the dimensions of the apertures on the electrodes are small in comparison to the

* Corresponding author at: Supercomputer Education and Research Centre, Indian Institute of Science, Bangalore 560012, India. Tel.: +91 80 22932979; fax: +91 80 23600135.
*E-mail addresses:* madhuri@isu.iisc.ernet.in (M. Chattopadhyay), amohanty@serc.iisc.ernet.in (A.K. Mohanty).

1387-3806/$ – see front matter © 2009 Elsevier B.V. All rights reserved.
doi:10.1016/j.ijms.2009.08.004

dimension of the trap, typically being less than 10% of the dimension of the trap. With the recent thrust to miniaturize these devices [4,2,6], it may not be possible to scale the apertures in the same proportion as the trap dimension. In such instances, the aperture dimension will be "large", going up to 20% or 30% of the trap dimension. In these miniaturized devices not only do apertures contribute more significantly to the field within the trap, but off-axis fields play a more important role in determining the dynamics of the trapped ions, since ion trajectories will have excursions well beyond the axis of the trap.

The contribution of apertures to the field within the trap has received only cursory attention in the mass spectrometry literature [12,15,7] and there is now a need, with the thrust towards miniaturization, to put it on a firmer theoretical footing. Our earlier effort [5] was able to extract the contribution of the aperture by subtracting the field in the vicinity of an aperture on an infinitely thin grounded plane from the field across this plane in the absence of the aperture. Extension of the same idea to fields at off-axis points, it turns out, involves significant new analysis with its own challenges, and is the subject of the present paper.

Our approach here is to assume that the field within 3D and 2D practical traps can be obtained by superposing (i) the field in a trap with apertures closed and (ii) the field contribution of the apertures. Accordingly, we write

$$E_{\text{withAperture}} = E_{\text{noAperture}} + E_{\text{dueToAperture}}. \tag{1}$$

For $E_{\text{noAperture}}$, we use direct numerical computation of the field using the boundary element method (BEM). To obtain an expression for $E_{\text{dueToAperture}}$, we take recourse to the problems of a circular hole and an infinite slit, for 3D and 2D geometries respectively, in an infinitely thin conducting ground plane with different constant perpendicular fields at faraway points on each side. It is possible to solve the resulting boundary value problems in closed form. The 3D solution we will use is adapted from Smythe [13]. Subtracting the field without the aperture from the field with the aperture on the conducting plane we obtain the contribution of the aperture. The theory is exact for a single hole or slit in an infinitely thin conducting ground plane. In practical traps the electrodes containing the apertures are not necessarily flat, have finite extent, and have nonzero thickness. Also, the faraway fields on both sides of the electrode are usually not constants. Yet, we will compute in this way some approximating fields which will match the exact fields very well.

In Section 2, we present the method for obtaining the fields within a trap with no apertures. Section 3 presents expressions for the off-axis fields in 3D traps, and Section 4 presents expressions for the off-axis fields in 2D traps. Section 5, Results and Discussion, verifies the utility of our expression by comparing it with numerically obtained fields. Section 6 presents a few concluding remarks.

## 2. Computation of $E_{\text{noAperture}}$

We have used the boundary element method (BEM), to compute the field numerically for any ion trap having a symmetric geometry. In the BEM, first the charge distribution on electrodes is determined from the known applied potential on the electrodes and then, the potential (and the field) at any point in space is computed from the charge distribution on the electrodes by the principle of superposition. A library developed by us allows an arbitrary 2D or 3D trap geometry to be defined and potentials on the trap electrodes to be specified.

To compute charge distribution on the electrodes, the electrode surfaces are divided into small regions or elements. Let $N$ be the total number of such elements, and let $v_i$ be the potential applied to $i$th element, and $g(i, j)$ (called the Green's function), be the potential at $i$th element due to unit charge at $j$ th element. The unknown charges must be such that the superposition of all their potentials on the $i$th element (for each $i$) must equal the applied potential there, namely $v_i$. Then the applied potentials $v_i$, $\quad i = 1 \ldots N$, must satisfy

$$\sum_{j=1}^{N} g(i,j)q_j = v_i, \quad \text{where} \quad i = 1 \ldots N. \tag{2}$$

Since the $v_i$ are specified, the $N$ unknown charges $q_j$ can be found by solving the linear system of $N$ simultaneous equations Eq. (2). Expressions for the Green's functions have been derived in Tallapragada et al. [15] for the 3D geometries, and in Krishnaveni et al. [8] for the 2D geometries. The computation of field and multipole coefficients from the numerically obtained charge distribution has also been discussed in those two papers. The details of the BEM solution are, therefore, discussed here no further.

## 3. Computation of $E_{\text{withHole}}$ for 3D traps

In Section 3.1, we will develop an expression for the contribution of a circular hole in an infinite ground plane, $E_{\text{dueToHole}}$. The expression for $E_{\text{withHole}}$ for 3D traps, which have electrodes of nonzero thickness, will follow in Section 3.2.

### 3.1. $E_{dueToHole}$ for a circular hole in an infinite ground plane

Consider an infinitely thin, grounded, conducting plane with different $z$-directed constant fields on either side as shown in Fig. 1(a). A hole of radius $a$, introduced in the conducting plane as shown in Fig. 1(b), will change the potential and the field close to the hole. We adapt the solution given in Smythe [13] to obtain an expression for the contribution of the hole to the potential at any point in space. The gradient of this expression will provide an expression for the field due to the hole.

In Fig. 1, the centre of the hole is at the origin. The potential without the hole is given by

$$U_{\text{noHole}}(z) = \begin{cases} -E_U z & \text{if } z \geq 0, \\ -E_L z & \text{if } z \leq 0, \end{cases} \tag{3}$$

where $E_U$ is the field above the electrode and $E_L$ is the field below the electrode.

The analysis for determining the potential when a hole is introduced (see [13]) is most conveniently carried out in oblate spheroidal coordinates $(\sigma, \tau, \phi)$, whose relation to the Cartesian coordinates $(x, y, z)$ is given by

$$x = a\sqrt{(1+\sigma^2)(1-\tau^2)}\cos\phi, \tag{4}$$

$$y = a\sqrt{(1+\sigma^2)(1-\tau^2)}\sin\phi, \tag{5}$$

$$z = a\sigma\tau. \tag{6}$$

$\sigma$, $\tau$, and $\phi$ have the ranges $-\infty < \sigma < \infty$, $0 \leq \tau \leq 1$, and $-\pi \leq \phi < \pi$. In this problem there is axial symmetry, so $\phi$ does not appear in

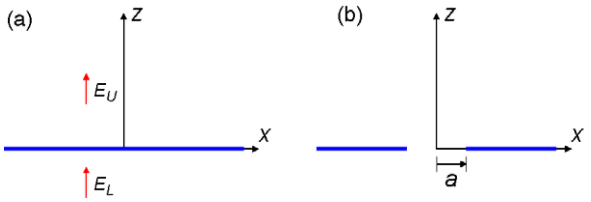


**Fig. 1.** Infinitely thin conducting sheet with (a) no hole, and (b) hole of radius $a$.

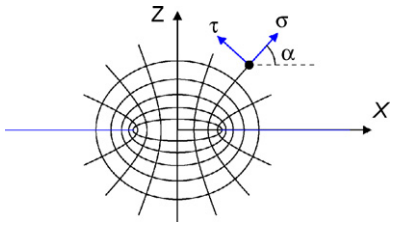


**Fig. 2.** Coordinate net for the spheroidal coordinate system.

the final expression which will now contain only $z$ and $\rho$, where

$$\rho = \sqrt{x^2 + y^2} = a\sqrt{(1+\sigma^2)(1-\tau^2)}. \tag{7}$$

Eqs. (6) and (7) express $z$ and $\rho$ in terms of $\sigma$ and $\tau$. Determination of $\sigma$ and $\tau$ from $\rho$ and $z$ can be accomplished in the following way. We compute $P = (\rho/a)^2 + (z/a)^2 - 1 = \sigma^2 - \tau^2$, $Q = (z/a)^2 = \sigma^2\tau^2$, and $R = \sqrt{P^2 + 4Q} = \sigma^2 + \tau^2$, then $\sigma = \text{sign}(z)\sqrt{(R+P)/2}$, and $\tau = z/(a\sigma)$. It should be noted that the calculation of $\sigma$ and $\tau$ requires only the ratios $\rho/a$ and $z/a$. This fact will be used in establishing the functional form of the electric field later.

We note that $\tau$ is nonnegative. $\tau = 0$ on the conducting plane, and $\tau = 1$ on the $z$ axis, where $\sigma = z/a$. Also $\sigma$ and $z$ have the same sign. Fig. 2 shows part of the coordinate net for the oblate spheroidal coordinate system superimposed on the outline of an infinitely thin conducting plane with a circular hole of radius $a$. Shown in the figure are the $\sigma$ and $\tau$ unit vectors at a point and the angle $\alpha$ the $\sigma$ unit vector makes with the radial ($\rho$) direction.

The scale factors [1] for the oblate spheroidal coordinates are

$$h_\sigma = a\sqrt{\frac{\sigma^2+\tau^2}{1+\sigma^2}}, \tag{8}$$

$$h_\tau = a\sqrt{\frac{\sigma^2+\tau^2}{1-\tau^2}}, \tag{9}$$

$$h_\phi = a\sqrt{(1+\sigma^2)(1-\tau^2)}. \tag{10}$$

The expression for the Laplace equation in terms of the oblate spheroidal coordinates is

$$\nabla^2 U = \frac{1}{a^2(\sigma^2+\tau^2)}\left[\frac{\partial}{\partial\sigma}\left((1+\sigma^2)\frac{\partial U}{\partial\sigma}\right) + \frac{\partial}{\partial\tau}\left((1-\tau^2)\frac{\partial U}{\partial\tau}\right) + \frac{\sigma^2+\tau^2}{(1+\sigma^2)(1-\tau^2)}\frac{\partial^2 U}{\partial\phi^2}\right] = 0. \tag{11}$$

We can carry out a separation of variables with the simplification that the potential, $U$, has no dependence on $\phi$ and write $U = S(\sigma)T(\tau)$. When this is done and substituted in Eq. (11) we obtain the two ODEs

$$\frac{d}{d\sigma}\left((1+\sigma^2)\frac{dS}{d\sigma}\right) - n(n+1)S = 0, \tag{12}$$

$$\frac{d}{d\tau}\left((1-\tau^2)\frac{dT}{d\tau}\right) + n(n+1)T = 0. \tag{13}$$

where the arbitrary constant $n$ is as yet undetermined.

Eq. (13) is the Legendre differential equation with argument $\tau$, while Eq. (12) is the Legendre differential equation with imaginary argument $i\sigma$. The possible solutions of Eq. (13) are the Legendre functions $P_n(\tau)$, and $Q_n(\tau)$, while those of Eq. (12) are $P_n(i\sigma)$, and $Q_n(i\sigma)$.

On the $z$ axis $\tau = 1$. So the solution $Q_n(\tau)$ for Eq. (13) is dropped here since this function has a singularity at $\tau = 1$. The asymptotic rate of growth of both $P_n(i\sigma)$ and $Q_n(i\sigma)$ as $|\sigma|$ tends to $\infty$ is like $\sigma^n$. Since in this problem the potential grows like $z = a\sigma\tau$ for large $|z|$, only the $n = 1$ solution needs to be considered. Thus

$$U_{\text{withHole}} = P_1(\tau)(AP_1(i\sigma) + BQ_1(i\sigma)) = \tau(Ai\sigma - B(\sigma\arctan\sigma + 1)). \tag{14}$$

where the constants $A$ and $B$ are to be determined from the conditions

$$\lim_{\sigma\to\infty}\frac{U_{\text{withHole}}}{a\sigma\tau} = -E_U, \tag{15}$$

and

$$\lim_{\sigma\to-\infty}\frac{U_{\text{withHole}}}{a\sigma\tau} = -E_L. \tag{16}$$

Thus $Ai - B\pi/2 = -aE_U$, and $Ai + B\pi/2 = -aE_L$, hence $Ai = -a(E_U + E_L)/2$, $B = a(E_U - E_L)/\pi$, and

$$U_{\text{withHole}} = -\frac{a(E_U+E_L)}{2}\sigma\tau - \frac{a(E_U-E_L)}{\pi}(\sigma\arctan\sigma + 1)\tau. \tag{17}$$

Since $z = a\sigma\tau$,

$$U_{\text{noHole}} = \begin{cases} -E_U a\sigma\tau & \text{if } \sigma \geq 0, \\ -E_L a\sigma\tau & \text{if } \sigma \leq 0. \end{cases} \tag{18}$$

Subtracting $U_{\text{noHole}}$ from $U_{\text{withHole}}$ we obtain the contribution of the hole to the potential, $U_{\text{dueToHole}}$, as

$$U_{\text{dueToHole}} = U_{\text{withHole}} - U_{\text{noHole}} = \frac{(E_U-E_L)}{2}a\left[\sigma\tau\,\text{sign}(\sigma) - \frac{2}{\pi}(\sigma\arctan\sigma + 1)\tau\right]. \tag{19}$$

We observe that, as might be intuitively expected, the contribution of the hole to the existing potential is proportional to $E_U - E_L$. Now the field components in the $\sigma$ and $\tau$ directions are found using

$$E_{\sigma,\text{dueToHole}} = -\frac{1}{h_\sigma}\frac{\partial U_{\text{dueToHole}}}{\partial\sigma} = -\frac{(E_U-E_L)\tau\sqrt{1+\sigma^2}}{2\sqrt{\sigma^2+\tau^2}}\left[\text{sign}(\sigma) - \frac{2}{\pi}\left(\arctan\sigma + \frac{\sigma}{1+\sigma^2}\right)\right], \tag{20}$$

and

$$E_{\tau,\text{dueToHole}} = -\frac{1}{h_\tau}\frac{\partial U_{\text{dueToHole}}}{\partial\tau} = -\frac{(E_U-E_L)\sqrt{1-\tau^2}}{2\sqrt{\sigma^2+\tau^2}}\left[|\sigma| - \frac{2}{\pi}(\sigma\arctan\sigma + 1)\right]. \tag{21}$$

Once the $\sigma$ and $\tau$ components are known, a coordinate transformation provides the $\rho$ and $z$ components. The angle $\alpha$ between the $\rho$ direction and the $\sigma$ direction is obtained from

$$\tan\alpha = \frac{\partial z/\partial\sigma}{\partial\rho/\partial\sigma} = \frac{\tau\sqrt{1+\sigma^2}}{\sigma\sqrt{1-\tau^2}}, \tag{22}$$

or,

$$\cos\alpha = \frac{\sigma\sqrt{1-\tau^2}}{\sqrt{\sigma^2+\tau^2}}, \tag{23}$$

$$\sin\alpha = \frac{\tau\sqrt{1+\sigma^2}}{\sqrt{\sigma^2+\tau^2}}. \tag{24}$$

Then we compute

$$E_{\rho,\text{dueToHole}} = E_{\sigma,\text{dueToHole}}\cos\alpha - E_{\tau,\text{dueToHole}}\sin\alpha, \tag{25}$$

$$E_{z,\text{dueToHole}} = E_{\sigma,\text{dueToHole}}\sin\alpha + E_{\tau,\text{dueToHole}}\cos\alpha. \tag{26}$$

The electric field thus found is a function of $\rho$, $z$, the hole radius $a$, and the difference between the fields $E_U - E_L$. We noted above that $E_{\text{dueToHole}}$ is proportional to $E_U - E_L$. Also, the three parameters $\rho$, $z$, and $a$ enter only as the two ratios $\rho/a$, and $z/a$. Thus the results obtained in this section can be expressed as

$$E_{\text{dueToHole}} = (E_U - E_L)F_{3D}(\rho/a, z/a), \tag{27}$$

where $F_{3D}$, a function of the two ratios $\rho/a$ and $z/a$, was derived above but is not written out in its entirety to keep the presentation uncluttered.

Eq. (27) is derived assuming the hole is at the origin. When the hole is at $z = z_0$, $z$ should be replaced by $z - z_0$ in Eq. (27). It should be noted that the discussion so far has been for a single hole in an infinitely thin ground plane. In an actual trap the endcaps will have nonzero thickness. In that case each endcap will be represented by two infinitely thin ground planes with a hole each. Thus for a practical trap, which has two endcaps of nonzero thickness, a total of four such contributions due to holes will be incorporated. It may be noted here that though the solution for the infinite thin grounded plane with a hole, as given above, is classical and rigorous, the approximation we are using it for, and in particular the four-time use of it as given below, is something of an engineering approximation, neither classical nor rigorous. The approximation therefore requires careful numerical verification before acceptance, and we will provide ample verification below.

### 3.2. Off-axis electric field in the axially symmetric (3D) trap

To elaborate the situation of a practical trap having top-bottom symmetry, we focus on Fig. 3. Fig. 3(a) shows the trap before the holes were introduced, while Fig. 3(b) shows the trap after bevelled holes were introduced in the endcaps. On the ejection axis, each endcap extends from a distance $z_0$ to a distance $z_1$. The radius at $|z| = z_0$ is $a_0$, while at $|z| = z_1$ is $a_1$. At the centre of the upper endcap, before the hole was introduced, the fields are also shown. The limiting value of the $z$ component of the field on the $z$ axis, as $z$ tends to $z_0$ from the centre of the trap, is denoted by $E_0$. The limiting value of the $z$ component of the field on the $z$ axis, as $z$ tends to $z_1$ from the exterior of the trap, is denoted by $E_1$. Because of the top-bottom symmetry, the corresponding fields on the lower endcap are $-E_0$ and $-E_1$, respectively. As in Chattopadhyay et al. [5] we approximate the hole in the endcap with nonzero thickness as two holes in two parallel infinitely thin ground planes and, as seen in Fig. 3, the two holes are at $z = z_0$, and at $z = z_1$. For the lower endcap the locations are $z = -z_0$, and $z = -z_1$. Table 1 shows the characteristics of the four ideal holes used to approximate the holes in a practical trap. When the contributions of the four holes are added

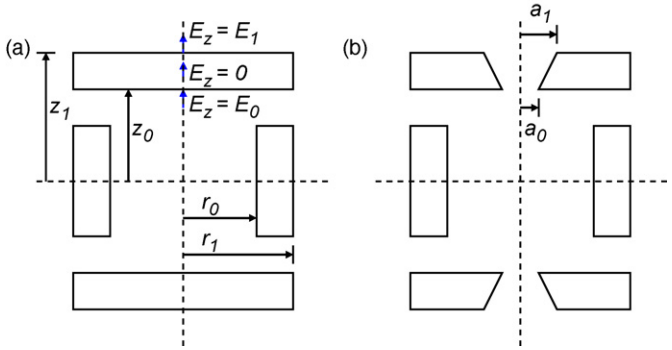


**Fig. 3.** Axially symmetric trap with thick endcaps.

**Table 1**
Locations, radii, and field differences for the four idealized holes corresponding to a practical trap shown in Fig. 3.

| Location | Radius | Upper field $E_U$ | Lower field $E_U$ | $E_U - E_L$ |
|---|---|---|---|---|
| $z = z_1$ | $a_1$ | $E_1$ | 0 | $E_1$ |
| $z = z_0$ | $a_0$ | 0 | $E_0$ | $-E_0$ |
| $z = -z_0$ | $a_0$ | $-E_0$ | 0 | $-E_0$ |
| $z = -z_1$ | $a_1$ | 0 | $-E_1$ | $E_1$ |

to the no-hole field we obtain the field with the hole, $E_{\text{withHole}}$, as

$$\begin{aligned} E_{\text{withHole}} = E_{\text{noHole}} \quad & +E_1\left(F_{3D}\left(\frac{\rho}{a_1}, \frac{z-z_1}{a_1}\right) + F_{3D}\left(\frac{\rho}{a_1}, \frac{z+z_1}{a_1}\right)\right) \\ & +(-E_0)\left(F_{3D}\left(\frac{\rho}{a_0}, \frac{z-z_0}{a_0}\right) + F_{3D}\left(\frac{\rho}{a_0}, \frac{z+z_0}{a_0}\right)\right). \end{aligned} \tag{28}$$

Here $E_{\text{noHole}}$ is numerically computed using the BEM. $F_{3D}$ is computed using the methods outlined in Section 3.1.

We now turn to 2D traps.

## 4. Computation $E_{\text{withSlit}}$ for 2D traps

In Section 4.1 we will develop an expression for the contribution of a slit in an infinite ground plane, $E_{\text{dueToSlit}}$. The expression for $E_{\text{withSlit}}$ for 2D traps, which have electrodes of nonzero thickness, is similar to the 3D case and will follow in Section 4.2.

### 4.1. $E_{dueToSlit}$ in the 2D trap for a slit in an infinite ground plane

Here too we begin our analysis by considering an infinitely thin grounded conducting plane. Fig. 4 shows two such planes, one with no slit and the other with a slit having half-width $a$. We assume the origin to be at the centre of the slit. The potential $U_{\text{noSlit}}$, without the slit, is given by

$$U_{\text{noSlit}} = \begin{cases} -E_U y & \text{if } y \geq 0, \\ -E_L y & \text{if } y \leq 0, \end{cases} \tag{29}$$

where $E_U$ is the field above the electrode and $E_L$ is the field below the electrode.

The analysis for determining the potential when a slit is introduced is simplified when we use elliptic coordinates $(\mu, \nu)$, related to the Cartesian coordinates $(x, y)$ by

$$x = a\cosh\mu\cos\nu, \tag{30}$$

$$y = a\sinh\mu\sin\nu. \tag{31}$$

Here $\mu$ and $\nu$ have the ranges $-\infty < \mu < \infty$, and $0 < \nu < \pi$, respectively. Eqs. (30) and (31) express $x$ and $y$ in terms of $\mu$ and $\nu$. Determination of $\mu$ and $\nu$ from $x$ and $y$ can be accomplished in the following way. We compute $P = (x/a)^2 + (y/a)^2 - 1 = \sinh^2\mu - \sin^2\nu$, $Q = (y/a)^2 = \sinh^2\mu\sin^2\nu$, and $R = \sqrt{P^2 + 4Q} = \sinh^2\mu + \sin^2\nu$. Then $\sinh\mu = \text{sign}(y)\sqrt{(R+P)/2}$, and $\sin\nu = \sqrt{(R-P)/2}$. It should be noted that the calculation of $\mu$ and $\nu$ requires only the ratios $x/a$ and $y/a$. We note that $\nu = 0$ on the conducting plane, and

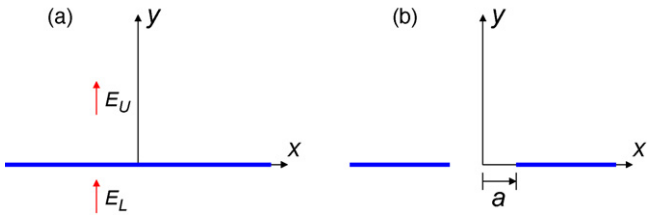


**Fig. 4.** Infinitely thin conducting sheet with (a) no slit, and (b) slit of half-width $a$.

$\nu = \pi/2$ on the $y$ axis, where $\sinh\mu = y/a$. Also $\mu$ and $y$ have the same sign. The scale factors for both $\mu$ and $\nu$ are identical and are

$$h_\mu = h_\nu = a\sqrt{\sinh^2\mu + \sin^2\nu}. \tag{32}$$

The expression for the Laplace equation in elliptic coordinates is

$$\nabla^2 U = \frac{1}{a^2(\sinh^2\mu + \sin^2\nu)}\left(\frac{\partial^2 U}{\partial\mu^2} + \frac{\partial^2 U}{\partial\nu^2}\right) = 0. \tag{33}$$

The solution, $U_{\text{withSlit}}$, which grows like $|y| = a|\sinh\mu\sin\nu|$ for large $|y|$, and is zero on the conducting plane with the slit is

$$U_{\text{withSlit}} = (A\cosh\mu + B\sinh\mu)\sin\nu, \tag{34}$$

where the constants $A$ and $B$ are to be determined from the conditions

$$\lim_{\mu\to\infty}\frac{U_{\text{withSlit}}}{a\sinh\mu\sin\nu} = -E_U, \tag{35}$$

and

$$\lim_{\mu\to-\infty}\frac{U_{\text{withSlit}}}{a\sinh\mu\sin\nu} = -E_L. \tag{36}$$

Thus $A + B = -aE_U$, and $-A + B = -aE_L$, hence $A = -a(E_U - E_L)/2$, and $B = -a(E_U + E_L)/2$, and

$$U_{\text{withSlit}} = -a\frac{E_U - E_L}{2}\cosh\mu\sin\nu - a\frac{E_U + E_L}{2}\sinh\mu\sin\nu. \tag{37}$$

Since $y = a\sinh\mu\sin\nu$,

$$U_{\text{noSlit}} = \begin{cases} -E_U a\sinh\mu\sin\nu & \text{if } \mu \geq 0, \\ -E_L a\sinh\mu\sin\nu & \text{if } \mu \leq 0. \end{cases} \tag{38}$$

Subtracting $U_{\text{noSlit}}$ from $U_{\text{withSlit}}$ we obtain the contribution of the hole to the potential, $U_{\text{dueToSlit}}$, as

$$\begin{aligned} U_{\text{dueToSlit}} &= U_{\text{withSlit}} - U_{\text{noSlit}} \\ &= \frac{(E_U - E_L)}{2}a\left[\sinh\mu\,\text{sign}(\mu) - \cosh\mu\right]\sin\nu \\ &= -\frac{(E_U - E_L)}{2}ae^{-|\mu|}\sin\nu. \end{aligned} \tag{39}$$

Once again, we note that the contribution is proportional to $E_U - E_L$. The field components in the $\mu$ and $\nu$ directions $E_{\mu,\text{dueToSlit}}$ and $E_{\nu,\text{dueToSlit}}$, respectively, are found using

$$E_{\mu,\text{dueToSlit}} = -\frac{1}{h_\mu}\frac{\partial U_{\text{dueToSlit}}}{\partial\mu} = -\frac{E_U - E_L}{2}\frac{\text{sign}(\mu)e^{-|\mu|}\sin\nu}{\sqrt{\sinh^2\mu + \sin^2\nu}}, \tag{40}$$

and

$$E_{\nu,\text{dueToSlit}} = -\frac{1}{h_\nu}\frac{\partial U_{\text{dueToSlit}}}{\partial\nu} = \frac{E_U - E_L}{2}\frac{e^{-|\mu|}\cos\nu}{\sqrt{\sinh^2\mu + \sin^2\nu}}. \tag{41}$$

Once the $\mu$ and $\nu$ components are known, a coordinate transformation provides the $x$ and $y$ components. The angle $\alpha$ between the $x$ direction and the $\mu$ direction is obtained from

$$\tan\alpha = \frac{\partial y/\partial\mu}{\partial x/\partial\mu} = \frac{\tan\nu}{\tanh\mu}, \tag{42}$$

or,

$$\cos\alpha = \frac{\sinh\mu\cos\nu}{\sqrt{\sinh^2\mu + \sin^2\nu}}, \tag{43}$$

$$\sin\alpha = \frac{\cosh\mu\sin\nu}{\sqrt{\sinh^2\mu + \sin^2\nu}}. \tag{44}$$

Then we compute $E_{x,\text{dueToSlit}}$ and $E_{y,\text{dueToSlit}}$, the field in the $x$ and $y$ directions, respectively, as

$$E_{x,\text{dueToSlit}} = E_{\mu,\text{dueToSlit}}\cos\alpha - E_{\nu,\text{dueToSlit}}\sin\alpha, \tag{45}$$

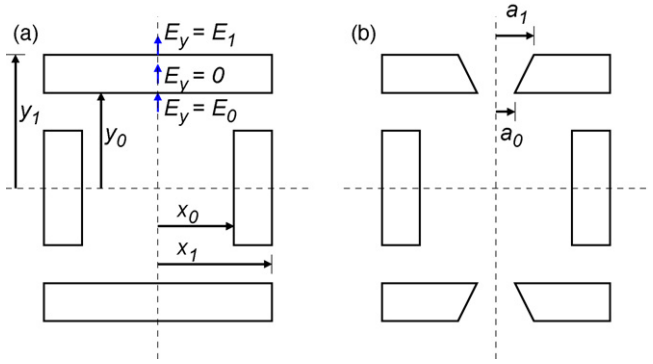


**Fig. 5.** 2D trap with slits in thick endcaps.

$$E_{y,\text{dueToSlit}} = E_{\mu,\text{dueToSlit}}\sin\alpha + E_{\nu,\text{dueToSlit}}\cos\alpha. \tag{46}$$

The electric field thus found is a function of $x$, $y$, the slit half-width $a$, and the difference between the fields $E_U - E_L$. We note that $E_{\text{dueToSlit}}$ is proportional to $E_U - E_L$. Also, the three parameters $x$, $y$, and $a$ enter only as the two ratios $x/a$, and $y/a$. Thus the results obtained in this section can be expressed as

$$E_{\text{dueToSlit}} = (E_U - E_L)F_{2D}\left(\frac{x}{a}, \frac{y}{a}\right), \tag{47}$$

where $F_{2D}$ is a function of $x/a$ and $y/a$, as described above but not written out in its entirety.

Eq. (47) is derived assuming the slit is at the origin. When the slit is at $y = y_0$, $y$ should be replaced by $y - y_0$ in Eq. (47). As discussed for the 3D case, here too for a practical trap a total of four such contributions due to slits will be needed.

### 4.2. Off-axis electric field in the 2D trap

For a practical trap having top-bottom symmetry, we focus on Fig. 5. Fig. 5(a) shows the trap without any slit on the electrodes, while Fig. 5(b) shows the same trap with bevelled slits in the electrodes. On the ejection axis each electrode extends from a distance $y_0$ to a distance $y_1$. The half-width at $|y| = y_0$ is $a_0$, while it is $a_1$ at $|y| = y_1$. At the centre of the upper electrode, before the slit was introduced, the fields are also shown. The limiting value of the $y$ component of the field on the $y$ axis, as $y$ tends to $y_0$ from the centre of the trap, is denoted by $E_0$. The limiting value of the $y$ component of the field on the $y$ axis, as $y$ tends to $y_1$ from the exterior of the trap, is denoted by $E_1$. Because of the top-bottom symmetry, the corresponding fields on the bottom electrode are $-E_0$ and $-E_1$, respectively. As in Chattopadhyay et al. [5], we approximate the slit in the electrode with nonzero thickness as two slits in two parallel infinitely thin ground planes. In Fig. 5 the slit in the upper electrode is considered as two slits in infinitely thin ground planes, one at $y = y_0$, and another at $y = y_1$. For the lower electrode the locations are $y = -y_0$, and $y = -y_1$. Table 2 shows the characteristics of the four ideal slits used to approximate the slits on electrodes with nonzero thickness in a practical trap. When the contributions of the

**Table 2**
Locations, half-widths, and field differences for the four idealized slits corresponding to a practical trap shown in Fig. 5.

| Location | Half-width | Upper field $E_U$ | Lower field $E_U$ | $E_U - E_L$ |
|---|---|---|---|---|
| $y = y_1$ | $a_1$ | $E_1$ | 0 | $E_1$ |
| $y = y_0$ | $a_0$ | 0 | $E_0$ | $-E_0$ |
| $y = -y_0$ | $a_0$ | $-E_0$ | 0 | $-E_0$ |
| $y = -y_1$ | $a_1$ | 0 | $-E_1$ | $E_1$ |

four slits are added to the no-slit field we obtain the field with the slit.

$$E_{\text{withSlit}} = E_{\text{noSlit}} + E_1\left(F_{2D}\left(\frac{x}{a_1}, \frac{y-y_1}{a_1}\right) + F_{2D}\left(\frac{x}{a_1}, \frac{y+y_1}{a_1}\right)\right) + (-E_0)\left(F_{2D}\left(\frac{x}{a_0}, \frac{y-y_0}{a_0}\right) + F_{2D}\left(\frac{x}{a_0}, \frac{y+y_0}{a_0}\right)\right). \quad (48)$$

Here $E_{\text{noSlit}}$ is computed numerically. $F_{2D}$ is computed using Eq. (47).

## 5. Results and discussion

The utility of Eqs. (25) and (26) to describe off-axis fields in the 3D traps and Eqs. (45) and (46) to describe off-axis fields in 2D traps will next be investigated. This will be done by comparing the fields obtained using our equations with those obtained numerically. For the 3D traps, we have taken up for investigation the QIT and the CIT geometries. For the 2D traps, we have investigated the LIT and the RIT geometries.

To estimate the fields using Eqs. (25) and (26) for the 3D geometries and Eqs. (45) and (46) for the 2D geometries, the $E_{\text{noAperture}}$ will need to be numerically obtained first. As has been mentioned earlier, this is done using the BEM. This also provides $E_0$ and $E_1$, along the principal axis. Once these fields have been computed numerically, the off-axis field for any aperture size can be approximated analytically using our expressions.

### 5.1. Layout of the figures

Since we are considering several trap designs, several aperture sizes for each design, and more than one display format for each aperture size, our graphical results below are necessarily rather detailed. For ease of reading, therefore, we adopt the following uniform format in Figs. 6–9. In each figure we present the geometry of the trap being investigated and a table adjacent to the figure provides the dimensions, in mm, of the different geometry parameters. The two subplots below the geometry diagram present the fields in the two directions along an arbitrary axis (indicated as $s$ in the geometry plot) which begins at the centre of the aperture and extends at an angle $135^0$ with the principal axis towards the adjacent electrode. In the case of the 3D traps, the plots correspond to $E_r$ and $E_z$ and in the case of 2D traps, the fields $E_x$ and $E_y$ are plotted along the arbitrary axis. These plots have been made for an aperture dimension which is 30% of the trap dimension.

Although an inspection of these field plots indicate a good match between the fields predicted by our expression when compared to fields obtained numerically, the match is demonstrated only along an arbitrarily chosen axis. To show that our expression performs well even in a larger region of the trap, we have chosen to plot "error" contours. For this we have chosen two different aperture sizes, one which is small, corresponding to 10% of the trap dimension, and the other which is large, corresponding to 50% of the trap dimension. For the purpose of comparing the field obtained using our expressions, $\vec{E}_{\text{est}}$, with that obtained numerically, $\vec{E}_{\text{num}}$,

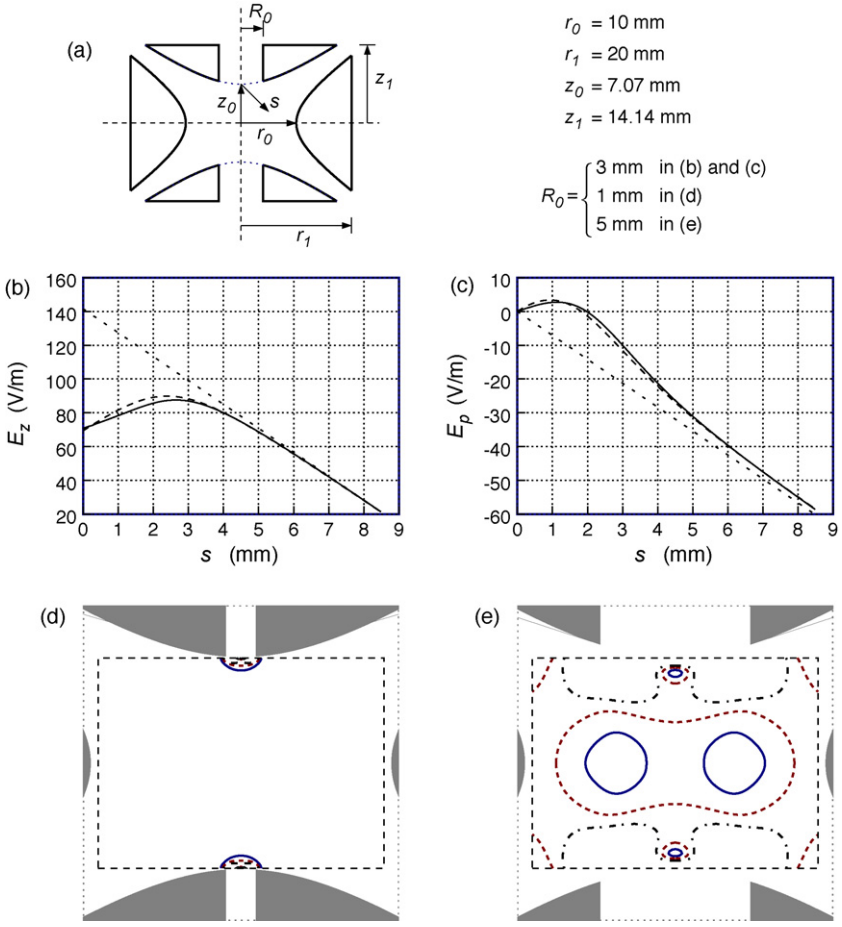


**Fig. 6.** (a) Cross-sectional view of the QIT. Comparison of (b) the $E_z$ field, and (c) the $E_\rho$ field, for a trap with hole radius of 3 mm. Dotted line: Field obtained using BEM with the holes artificially closed. Solid line: Field obtained using BEM for a trap with holes. Dashed line: Field obtained using our expression. Contour plot of the relative percentage errors in field for the QIT with (d) 1 mm hole radius, and (e) 5 mm hole radius. (Solid contour: 1%, Dashed contour: 2%, Dot-Dash contour: 3%.)

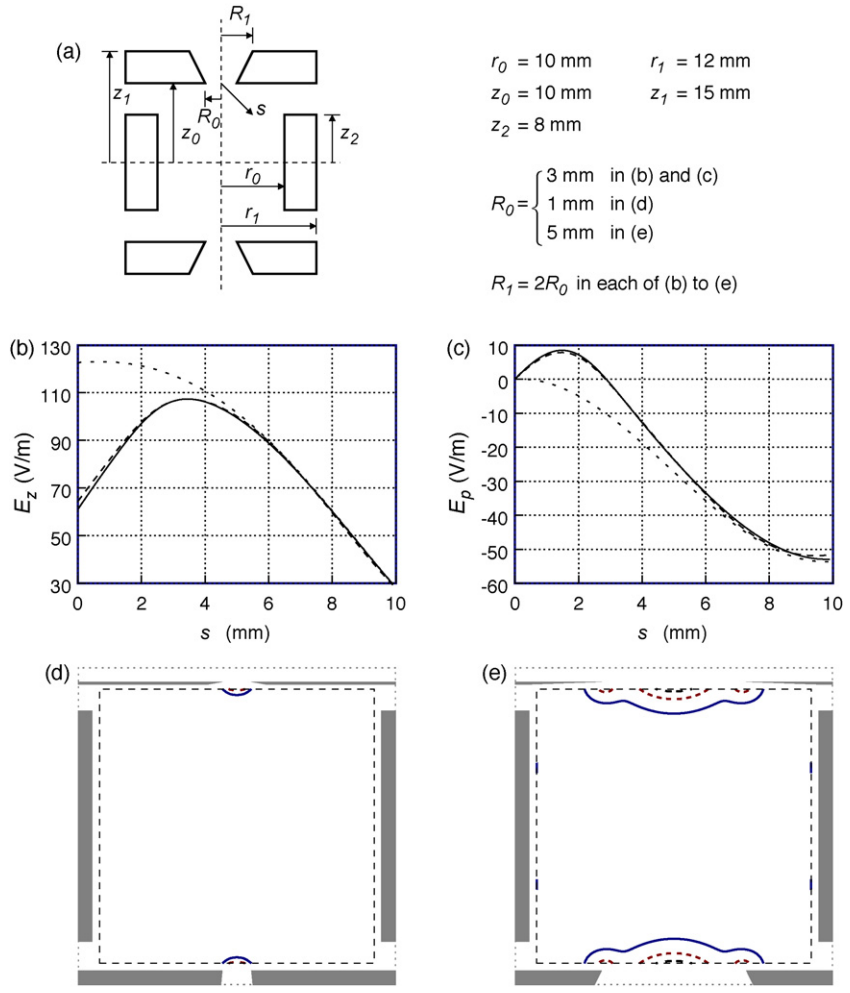


**Fig. 7.** (a) Cross-sectional view of the CIT. Comparison of (b) the $E_z$ field, and (c) the $E_\rho$ field, for a trap with hole radius of 3 mm. Dotted line: Field obtained using BEM with the holes artificially closed. Solid line: Field obtained using BEM for a trap with holes. Dashed line: Field obtained using our expression. Contour plot of the relative percentage errors in field for the CIT with (d) 1 mm hole radius, and (e) 5 mm hole radius. (Solid contour: 1%, Dashed contour: 2%, Dot-Dash contour: 3%.)

we show contour plots of the *relative percentage error*, $\epsilon$, defined as

$$\epsilon = \frac{|\vec{E}_{\text{num}} - \vec{E}_{\text{est}}|}{|\vec{E}_{\text{num}}|} \times 100 \tag{49}$$

We trace contours corresponding to relative percentage errors of 1%, 2%, and 3%. Although in some contour plots it will be seen that the relative percentage error is below 1% over a large region inside the trap, we have chosen not to trace contours with smaller errors, since we consider 1% error to be reasonably small for most engineering applications.

The region over which these relative percentage error contours are computed is shown in each figure by a dashed rectangle. This region has been arbitrarily chosen to include the region of stable ion motion. Beyond this region, close to and within the aperture, our simple analysis may not be adequate.

### 5.2. Axially symmetric (3D) traps

#### 5.2.1. The QIT

Fig. 6 presents the geometry of the QIT, the fields in $r$ and $z$ directions along the arbitrary axis, $s$, in a trap in which the aperture is 30% of the trap dimension and the error contours for a trap with aperture dimensions of 10% and 50% of the trap dimension. For these simulations, the ring electrode was kept at unit positive potential and the endcaps were grounded. The dimensions of the trap that we have investigated are given in the table adjacent to the geometry of the trap.

$E_{\text{noHole}}$ in Eqs. (25) and (26) have been estimated numerically [15]. These computation yield values of $E_0$ and $E_1$ as 141.5875 and −20.3333 V/m, respectively.

In Fig. 6(b) and (c), the axial field ($E_z$) and the radial field ($E_r$) are plotted along the ordinate in V/m, for a hole radius of 3 mm (corresponding to 30% of the trap dimension) and the off-axial distance is plotted along the abscissa in mm. In these plots, the field components obtained numerically are plotted using continuous lines and those obtained by our approximation are plotted using dashed lines. The numerically obtained field components in the same trap with the apertures artificially closed are plotted using dotted lines. It may be seen that there is a marginal difference between the analytically estimated fields and numerically obtained fields near the hole. At all other points, our analytical approximations match well with the numerically obtained fields.

Fig. 6(d) and (e) are the contour plots of the error in estimating the field by our expression compared to the numerically obtained field and correspond to traps in which the aperture dimension is 1 and 5 mm corresponding to 10% and 50% of trap dimension, respectively. In the figures, the solid, dashed, and dot-dashed contours correspond to relative percentage error values of 1%, 2%, and 3%, respectively. For a hole radius of 1 mm, the error occurs only near to the holes as shown by the contour plot in Fig. 6(d). For the trap

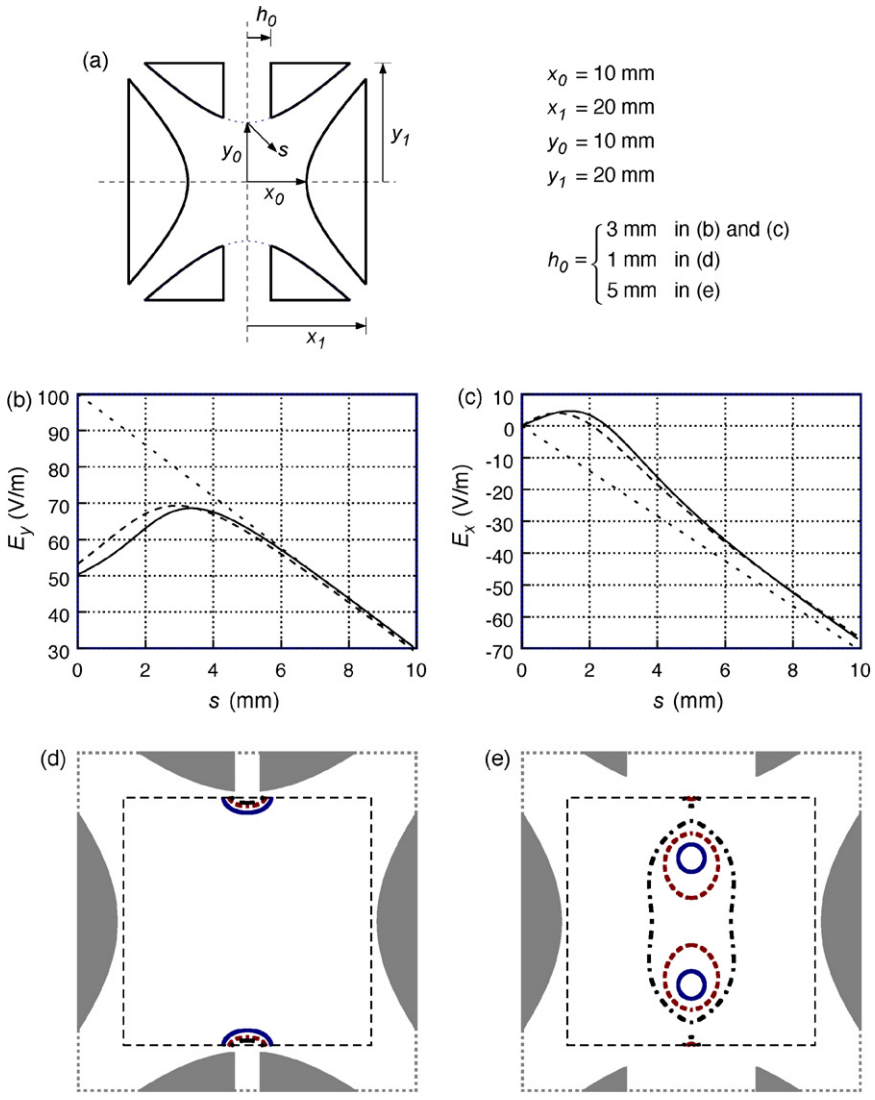


**Fig. 8.** (a) Cross-sectional view of the LIT. Comparison of (b) the $E_y$ field, and (c) the $E_x$ field, for a trap with slit half-width of 3 mm. Dotted line: Field obtained using BEM with the slits artificially closed. Solid line: Field obtained using BEM for a trap with slits. Dashed line: Field obtained using our expression. Contour plot of the relative percentage errors in field for the LIT with (d) 1 mm slit half-width, and (e) 5 mm slit half-width. (Solid contour: 1%, Dashed contour: 2%, Dot-Dash contour: 3%.)

with hole radius of 5 mm, 1% contours are seen close to the trap centre (two regions), as well as close to the aperture. At the centre of the trap itself, the relative percentage error is within 2%, with larger relative percentage errors of 3% appearing close to the holes.

### 5.2.2. The CIT

Fig. 7 presents the schematic diagram of CIT geometry, the axial and radial fields along the arbitrary axis, *s*, in a trap where the aperture is 30% of the trap dimension and the error contour plots with aperture dimensions of 10% and 50% of the trap dimension. The table associated with the geometry of the trap under investigation, shows the dimensions of the trap parameters in mm. In these simulations, the ring electrode was kept at unit positive potential while the endcap electrodes were kept at ground potential.

$E_{\text{noHole}}$ in Eqs. (25) and (26) have been estimated numerically [15]. These computation yield values of $E_0$ and $E_1$ as 122.6764 and −10.892 V/m, respectively.

Here too, in Fig. 7(b) and (c), the axial field ($E_z$) and the radial field ($E_r$) are plotted along the ordinate in V/m, with a hole radius of 3 mm and the off-axial distance is plotted along the abscissa in mm. In these plots, the field components obtained numerically are plotted using continuous lines and those obtained by our approximation are plotted using dashed lines. The numerically obtained field components in the same trap with the apertures artificially closed are plotted using dotted lines.

A small deviation is noticed between the analytical and numerical fields along *z* direction near the hole. At all other points, the match between the two fields is good.

Fig. 7(d) and (e) present the contour plots for error in off-axis field computation using our expressions compared to numerical computed field for hole radii of 1 and 5 mm, respectively. In the figures, the solid, dashed, and dot-dashed contours correspond to relative percentage error values of 1%, 2%, and 3%, respectively. It can be seen that for both the 1 and the 5 mm cases the prediction of our analytical expression is very good, with the 1% contour occuring only close to the holes. Thus in a large region of the trap, our expression deviates from numerically obtained value by less than 1%.

## 5.3. 2D traps

### 5.3.1. The LIT

Fig. 8 presents the geometry of LIT, the fields in the *x* and *y* directions along the arbitrary axis *s* in a trap in which aperture is

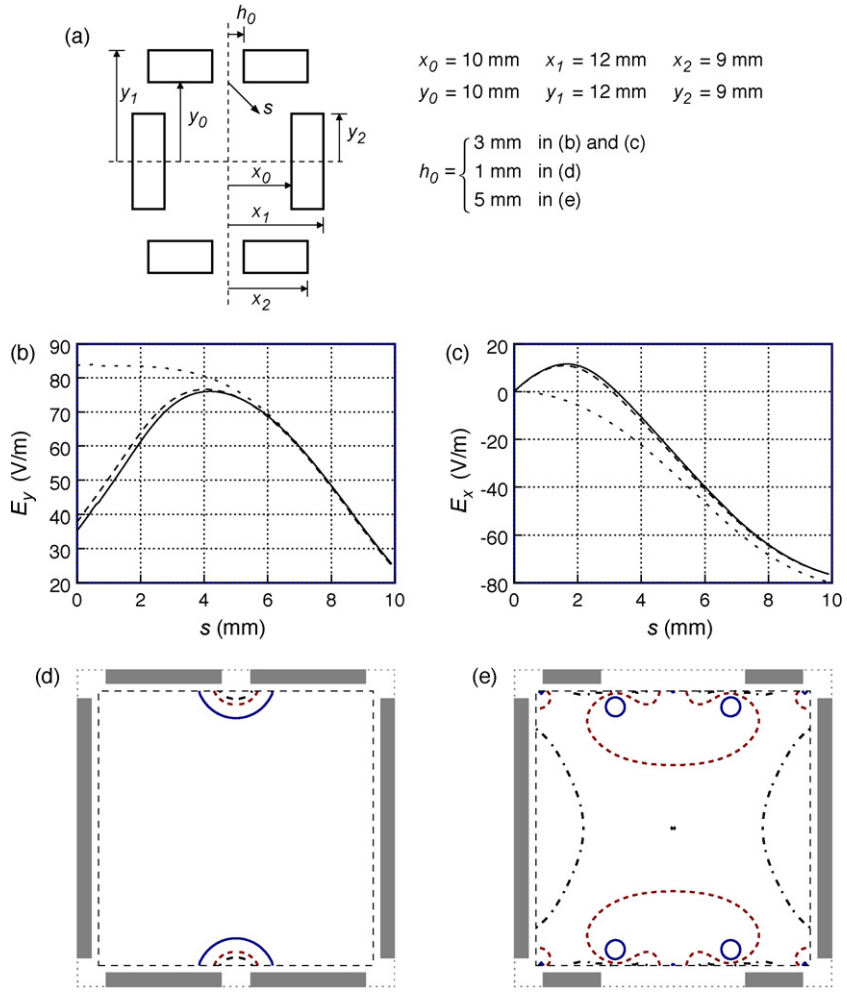


**Fig. 9.** (a) Cross-sectional view of the RIT. Comparison of (b) the $E_y$ field, and (c) the $E_x$ field, for a trap with slit half-width of 3 mm. Dotted line: Field obtained using BEM with the slits artificially closed. Solid line: Field obtained using BEM for a trap with slits. Dashed line: Field obtained using our expression. Contour plot of the relative percentage errors in field for the RIT with (d) 1 mm slit half-width, and (e) 5 mm slit half-width. (Solid contour: 1%, Dashed contour: 2%, Dot-Dash contour: 3%.).

30% of the trap dimension and the error contours for the trap with aperture dimensions of 10% and 50% of the trap dimension. The dimensions of the trap parameters are given in the table adjacent to the trap geometry. In our simulations, one pair of electrodes (along the $x$-axis) was kept at unit positive potential, and the other pair of electrodes was grounded. $E_{\text{noSlit}}$ in Eqs. (45) and (46) have been estimated numerically [8]. These computation yield values of $E_0$ and $E_1$ as 100.131 and −18.38 V/m, respectively.

In Fig. 8(b) and (c), the fields ($E_x$ and $E_y$) are plotted along the ordinate in V/m, with an aperture dimension of 30% of the trap dimension and the off-axial distance from the middle ($y_0$,0) of the slit in the inner surface of the top electrode, is plotted along the abscissa in mm for a slit with half-width of 3 mm (corresponding to 30% of the trap dimension). In these plots, the field components obtained numerically are plotted using continuous lines and those obtained by our approximation are plotted using dashed lines. The numerically obtained field components in the same trap with the apertures artificially closed are plotted using dotted lines.

There are marginal differences between the analytically estimated fields and numerically obtained fields in both cases. These differences are due to the change in dimension of $y_0$ which occurs when the aperture width is increased on the hyperbolic electrodes. This difference could be nullified by inserting the actual value of $y_0$ in the analytical expressions.

The contour plots for the errors with a slit half-width of 1 and 5 mm are shown in Fig. 8(d) and (e), respectively. In the figures, the solid, dashed, and dot-dashed contours correspond to relative percentage error values of 1%, 2%, and 3%, respectively. With a slit half-width of 1 mm, the contour plots indicate good agreement between the two computations as error corresponding to 1% occurs only near to the slits as shown in Fig. 8(d). However, for a slit half-width of 5 mm in Fig. 8(e), the picture is similar to that of the QIT. Here however, close to the centre of the trap, the error is greater than that for the QIT.

### 5.3.2. The RIT

Fig. 9 presents the geometry of RIT, the $x$ and $y$ directional fields along the arbitrary axis, $s$, for slit half-width of 30% of the trap dimension and the error contours for a trap with slit half-widths of 10% and 50% of the trap dimensions. In these simulations the electrode pair with no slit have been kept at unit positive potential while the electrode pair with slits have been kept at ground potential.

$E_{\text{noSlit}}$ in Eqs. (45) and (46) have been estimated numerically [8] which yield values of $E_0$ and $E_1$ as 83.7133 and −32.8307/,V/m, respectively.

Using Eqs. (45) and (46), we plot the fields $E_x$ and $E_y$ for a slit half-width of 3 mm in Fig. 9(b) and (c) respectively. The ordinate shows the field strengths in V/m and the abscissa indicates the

off-axial distance in mm. In these plots, the field components obtained numerically are plotted using continuous lines and those obtained by our approximation are plotted using dashed lines. The numerically obtained field components in the same trap with the apertures artificially closed are plotted using dotted lines. The analytical estimation shows a good match with the numerically obtained fields.

The contour plots as shown in Fig. 9(d) and (e), correspond to the errors in estimating the field by our analytical approximation compared to the numerically obtained field for slit half-widths of 1 and 5 mm. In the figures, the solid, dashed, and dot-dashed contours correspond to relative percentage error values of 1%, 2%, and 3%, respectively. With a slit half-width of 1 mm, the 1% contour plot (Fig. 9(d)), is seen only close to the slit, indicating that within a large region of the trap, our expression predicts the field with reasonable accuracy. For the trap having a slit half-width of 5 mm, the accuracy is less, with the relative percentage error in the region close to the trap centre being within 3%.

## 6. Concluding remarks

In this paper we have developed an analytical expression for off-axis fields, $E_{\text{withHole}}$ for 3D traps and $E_{\text{withSlit}}$ for 2D traps, for ion trap mass analyzers with apertures on their electrodes. The expression consists of two terms. Of these, the first ($E_{\text{noAperture}}$) is the field in a trap with apertures closed: this is computed numerically using the BEM. The second ($E_{\text{dueToAperture}}$) is the contribution of the aperture to the field in the vicinity of the aperture. The summation of $E_{\text{noAperture}}$ and $E_{\text{dueToAperture}}$ gives the expression for off-axis fields.

The expressions for $E_{\text{withHole}}$ for 3D traps and $E_{\text{withSlit}}$ for 2D traps have been verified by direct comparison with BEM numerics for several geometries and aperture sizes. For 3D traps, the QIT and the CIT geometries have been investigated and for 2D traps, the LIT and the RIT geometries have been investigated. In all these geometries, comparison has first been done along an arbitrary axis for a trap in which the aperture is 30% of the trap dimension. Subsequently, relative percentage error contours corresponding to 1%, 2%, and 3% have been plotted for two aperture dimensions, viz., 10% and 50% of the trap dimensions.

An inspection of the contour plots for traps with aperture dimension of 10% of the trap dimension indicates that our analytical expression performs well over a large region of the trap. It is only close to the apertures that the errors increase, and here too the agreement is within 3%. For the case of traps with aperture 50% of the trap dimension, on the other hand, the picture appears to be more complicated. Not only are the variations in the field not monotonic, but islands of variable performance of our expression are observed. We are unable to explain this lack of monotonicity using our theory. In spite of this, the overall agreement between the field obtained using our analytical expressions and the field obtained numerically is seen to be good, even when the aperture is far from small.

The methodology that we have developed here can be applied to near-hole fields in traps which have hitherto not been amenable to analytical treatment. An obvious example of such a trap is the now famous commercial Paul trap [14] which has *asymmetric* holes on the two endcap electrodes and which also has a so-called stretch. Although we have here studied traps with top-and-bottom symmetry, the theory developed works even in the absence of such symmetry. This in turn opens the way for studying fields in what might be called *designer traps* with special purpose holes in arbitrary locations on the electrodes, possibly to meet specific requirements of future experimental research.

## Acknowledgement

We thank Anindya Chatterjee and A.G. Menon for discussions and suggestions on the manuscript, and thank an anonymous reviewer of our earlier work [5] for pointing us in this direction.

## References

[1] G.B. Arfken, Mathematical Methods for Physicists, Academic Press, London, 2005.
[2] D.E. Austin, D. Cruz, M.G. Blain, Simulations of ion trapping in a micrometer-sized cylindrical ion trap, Journal of American Society of Mass Spectrometry 17 (2006) 430–441.
[3] M.E. Bier, J.E.P. Syka, U.S. Patent 5,420,425 (1995).
[4] M.G. Blain, S.R. Leah, D. Cruz, D.E. Austin, G. Wu, W.R. Plass, R.G. Cooks, Towards the hand-held mass spectrometer: design considerations, simulation, and fabrication of micrometer-scaled cylindrical ion traps, International Journal of Mass Spectrometry 236 (2004) 91–104.
[5] M. Chattopadhyay, N.K. Verma, A.K. Mohanty, Composite field approximation for ion traps with apertures on electrodes, International Journal of Mass Spectrometry 282 (2009) 112–122.
[6] D. Cruz, J. Change, M. Fico, A. Guymon, D.E. Austin, M.G. Blain, Design, microfabrication, and analysis of micrometer-sized cylindrical ion trap arrays, Review of Scientific Instruments (2009) 015107-1–0151079-0151079.
[7] H. Koizumi, W.B. Whitten, P.T. Reilly, E. Koizumi, The effect of endcap electrode holes on the resonant ejection from an ion trap, International Journal of Mass Spectrometry 281 (2009) 108–114.
[8] A. Krishnaveni, N.K. Verma, A.G. Menon, A.K. Mohanty, Numerical observation of preferred directionality in ion ejection from stretched rectilinear ion traps, International Journal of Mass Spectrometry 275 (2008) 11–20.
[9] D.B. Langmuir, R. Langmuir, H. Shelton, R.F. Wuerker, Containment device, U.S. Patent 3,065,640 (1962).
[10] Z. Ouyang, G. Wu, Y. Song, H. Li, W.R. Plass, R.G. Cooks, Rectilinear ion trap: concepts, calculations, and analytical performance of a new mass analyser, Analytical Chemistry 76 (2004) 4595–4605.
[11] W. Paul, H. Steinwedel, U.S. Patent 2939952 (1960).
[12] W.R. Plass, H. Li, R.G. Cooks, Theory, simulations and measurement of chemical mass shifts in RF quadrupole ion traps, International Journal of Mass Spectrometry 228 (2003) 237–267.
[13] W.R. Smythe, Static and Dynamic Electricity, McGraw-Hill, New York, 1950.
[14] J.E.P. Syka, Commercialization of the quadrupole ion trap, in: R.E. March, J.F.J. Todd (Eds.), Practical Aspects of Ion Trap Mass Spectrometry, vol. 1, CRC Press, New York, 1995, pp. 169–205.
[15] P.K. Tallapragada, A.K. Mohanty, A. Chatterjee, A.G. Menon, Geometry optimization of axially symmetric ion traps, International Journal of Mass Spectrometry 264 (2007) 38–52.
[16] G. Wu, R.G. Cooks, Z. Ouyang, Geometry optimization for the cylindrical ion trap: field calculations, simulations and experiments, International Journal of Mass Spectrometry 241 (2005) 119–132.